Coronal Mass Ejections: Masses, Dynamics and Shock Kinematics

A dissertation submitted to the University of Dublin
for the degree of *Philosophiæ Doctor (PhD)*

Eoin P. Carley
Trinity College Dublin, December 2013

Declaration

I declare that this thesis has not been submitted as an exercise for a degree at this or any other university and it is entirely my own work.

I agree to deposit this thesis in the University's open access institutional repository or allow the library to do so on my behalf, subject to Irish Copyright Legislation and Trinity College Library conditions of use and acknowledgement.

Name: Eoin Carley

Signature: .... **Date:** ....

Summary

Coronal mass ejections (CMEs) are large-scale eruptions of magne-tized plasma from the low solar atmosphere into interplanetary space. With energies of up to 10^{26} J, they are the most energetic eruptive phe-nomena in the solar system and are also the driver of plasma shocks from the corona into the heliosphere. Despite many years of study, the nature of the forces governing their eruption, and the kinemati-cal behavior of the resulting shock, remain poorly understood. This thesis will presents the first accurate calculation of the magnitude of the total force on a CME. I will also show a previously unseen plasma shock behavior that sheds new light into the kinematical nature of CME-driven shocks in the corona.

In the past, measurement of the forces governing the propagation of CMEs have been hindered by highly uncertain estimates of the total mass of the ejection. The primary source of uncertainty is the unknown position and geometry of the CME, leading to an erroneous treatment of the Thomson scattering equations which are used to estimate the mass. Geometrical uncertainty on the CMEs position and size has primarily been due to observations of the eruption from a single vantage point. However, with the launch of the STEREO spacecraft, the two viewpoints can be exploited to derive the CMEs position and size, ultimately resulting in mass uncertainty that is both reliably quantified and much reduced. These much better estimates for the mass can then be combined with kinematical results that are also more reliable and hence lead to the first reliable quantification of the total force acting on the CME.

This thesis will present the method by which mass values derived from the STEREO coronagraphs, and the uncertainties reliably quantified. Combining this with a previous kinematical analysis, the mechanical energies and total force on the CME is derived. Using the magnetohydrodynamical equation of motion, the relative sizes of the forces at each stage in the CME propagation are estimated, revealing the Lorentz force is the largest source of CME acceleration early in its propagation. This analysis also leads to a reliable observational estimate of size of this Lorentz force.

CMEs often erupt at speeds in excess of the local MHD wave speeds in the corona. Traveling in excess of Mach 1, they often drive shocks which can have a variety of manifestations, from radio bursts to the propagation of bright pulse seen in extreme ultraviolet (EUV) images. Despite these myriad shock phenomena being observed for decades, the relationship between them remains unknown. Chapters X and Y of this thesis, will describe the construction of instrumentation to observe high time sampling spectroscopy of these radio bursts. These observations are combined with high cadence radio and EUV images to reveal the presence of a shock driven by the expansion of the CME flank that resulted in both the EUV pulse and radio burst. Furthermore, the radio spectra evidence for particle acceleration at this shock is presented, revealing the shock was capable of producing a bursty acceleration of near-relativistic electrons. This previously unseen behavior sheds new light on the physics governing radio burst generation and the relationship to CMEs and EUV pulses.

For my parents.

Acknowledgements

Some sincere acknowledgements...

List of Publications

1. **Carley, E. P.**, MacAteer, R. T. J., & Gallagher, P. T.
   "Coronal Mass Ejection Masses, Energies, and Force Estimates Using *STEREO*",
   The Astrophysical Journal, Volume 752, Issue 1, article id. 36, 8 pp. (2012).

2. Zucca, P., **Carley, E. P.**, McCauley, J., Gallagher, P. T. ,Monstein, C., &
   MacAteer, R. T. J.,
   "Observations of Low Frequency Solar Radio Bursts from the Rosse Solar-
   Terrestrial Observatory",
   Solar Physics, Volume 280, Issue 2, pp.591-602. (2012).

3. **Carley, E. P.**, Long, D. M., & Gallagher, P. T.
   "Shock Acceleration of Energetic Particles in the Solar Atmosphere",
   Some Journal, Volume X, Issue Y, article id. (2013)

4. Zucca, P., **Carley, E. P.**, Bloomfield, S. D., & Gallagher, P. T.
   "Density and Alfvén....",
   Some Journal, Volume X, Issue Y, article id. (2013)

5. Bloomfield, S. D., **Carley, E. P.**,
   "A Comprehensive Overview of the 2011 June 7 Solar Storm",
   Astronomy & Astrophysics, Volume X, Issue Y, article id. (2013)

Contents

List of Figures

List of Tables

1

Introduction

The Sun has long been the focus of humanity's curiosity. Throughout history it has been the harbinger of new religions, philosophies, and sciences. It has changed our understanding of our place in the Universe and allowed us to push forward the frontiers of stellar astronomy. Although our understanding of the Sun is nowadays more advanced, the curiosity we hold for it has not changed since the very early humans. Now, we understand the Sun is a star similar to any other in its class, currently going through a relatively unchanging 11 year cycle of activity that is extremely rich in physical complexity. The study of such complex phenomena has yielded immeasurable advances in many areas of physics such as spectroscopy, plasma physics, magnetohydrodynamics (MHD), particle physics, to name but a few. Although some of these sciences have grown over decades (or even centuries) they are still incomplete. I hope this theses, in some small way, will contribute to the continuing growth of these sciences and to the understanding of our nearest star.

1.1 The Sun

The Sun is our nearest star, located 1.49×10^6 km from Earth at the centre of our solar system. Located on the main sequence of the Hetzpring-Russel (HR) diagram, it has a spectral class of G2V, with a luminosity of $L_\odot = (3.84 \pm 0.04) \times 10^{26}$ W, mass of $M_\odot = (1.989 \pm 0.0003) \times 10^{30}$ kg and radius of $R_\odot = (6.959 \pm 0.007) \times 10^8$ m (Foukal, 2004). It was born approximately 4.6×10^9 years ago when a giant molecular cloud underwent gravitational collapse and began hydrogen nuclear fusion at its centre (reference). The energy produced from this fusion resulted in enough pressure to counteract gravitational contraction and bring about a hydrostatic equilibrium, allowing the young star to reach a stability that is sustained today. It is estimated the Sun will maintain this stability for another 5 billion years, at which point, it will move off the main sequence and into a red giant phase. During this later part of its life, it will grow in size to 100 times its current radius and begin nuclear burning of heavier elements such as carbon and oxygen. Once carbon burning in the core has ceased it can no longer sustain nuclear fusion of heavier elements, resulting in a gravitational instability that will eventually lead to a stellar nova. This nova will result in the loss of the outer envelopes and ultimately the Sun's death, leaving behind a compact and dense white-dwarf.

Until such time, the Sun will remain on the main sequence in a regular state of hydrogen fusion in its core. The energy released during this process is the ultimate source of light and all energetic activity that we observe from Earth and beyond. Before we can understand how this energy manifests in the solar atmosphere as a variety of energetic phenomena, it is important to understand how the energy is generated and transported through its interior and finally released into its atmosphere and interplanetary space.

1.1.1 Solar Interior

The theoretical development on how the solar interior is structured and how it behaves has been through what is known as the 'standard solar model' or SSM. The SSM is a grouping of theories that described how the Sun was formed, how it maintains its stability, how it generates energy, and how this energy is transported

through its interior and released at the surface. Much of the major developments of this theory have been in the 20th century, due mainly to the pioneering experiments in solar neutrino physics and helioseismsology. Hence, the development of the SSM has mainly been through a refinement of the theory based on these observational fields. Although the SSM has increased in sophistication, its four main aspects remain the most general framework for describing the behavior of the solar interior.

The SSM firstly states that the Sun was born from the gravitational collapse of a primordial gas of hydrogen, helium, and traces of other heavy elements. Secondly, it maintains its structural stability via a hydrostatic equilibrium such that the gravitational force is balanced by a pressure gradient ($\nabla P = -\rho g$) at each radial distance inside the star. The third main aspect of the SSM involves the source of the Sun's energy. Much of the early ideas proposed during the 19th century involved some form of chemical reaction or energy released during a slow gravitational contraction. However, during the first half of the 20th century the theory that the Sun is at least as old as the Earth began to come into focus. The idea of the Sun being more than 4.5 billion years old prompted the question of what energy source could sustain the Sun's luminosity for such a length of time. It was soon realised that thermonuclear fusion must be the source of such energy, and, as a result, it should be possible to observe the neutrino products of this fusion. Hence, starting in the 1950s a number of pioneering neutrino physics experiments were developed in an attempt to detect solar-generated neutrinos at Earth. These pioneering experiments, as well as there more sophisticated counterparts today, confirm much of the theories on solar core energy generation.

From the 1950s onwards there has been a confirmed detection of neutrinos generated in a hydrogen fusion process, namely the proton-proton or 'pp'-chain, in the solar core. In this process, four protons are fused to form a helium nucleus. This can occur in a variety of ways, but at the Sun's core temperature of 15 MK, the dominant reaction is the pp 1 chain given by

$$^1_1\text{H} +^1_1\text{H} \rightarrow\ ^2_1\text{H} + e^+ + \nu_e \tag{1.1}$$

$$^2_1\text{H} +^1_1\text{H} \rightarrow \ ^3_2\text{He} + \gamma \tag{1.2}$$

$$^3_2\text{He} +^3_2\text{He} \rightarrow \ ^4_2\text{He} + 2^1_1\text{H} \tag{1.3}$$

where $^1_1$H is a hydrogen nucelus, $^2_1$H is deuterium, $^3_2$He is tritium, $^4_2$He is helium, e^+ is a positron, ν_e is an electron neutrino, and γ is a gamma ray photon. Reactions (1.1) and (1.2) must happen twice for (1.3) to occur. Taking this into account, the entire process may be summarised as

$$4^1_1\text{H} \rightarrow \ ^4_2\text{He} + 2e^+ + 2\nu_e + 2\gamma \tag{1.4}$$
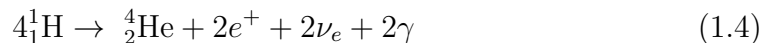
liberating 4.2×10^{-12}J of energy, with $\sim 2.4\%$ of the energy carried away by the neutrinos. This particular form of the pp-chain (pp 1) occurs in 86% of the cases (Turck-Chièze & Couvidat, 2011). However, there are other reactions capable of producing He from H catagorized into pp II, pp III etc, which each involve production of $^7_4$Be and $^8_5$B. The initial neutrino detections at Earth were the result of the pp III reaction which involves the creation of $^8_5$B, followed by a decay to $^8_4$Be, a positron, and an electron neutrino (Davis *et al.*, 1968). These early detections and the results of more recent experiments such as the SuperKamiokande (Fukuda *et al.*, 1998) show that the expected neutrino flux given by the standard solar model is smaller than the observed. This deficit in in neutrino flux observations became the famed 'solar neutrino problem' during the 1970s. One of the proposed explanations for the process was via an oscillation of the neutrino amongst three sets of 'flavors' i.e., the neutrino can be either an electron ν_e, muon ν_μ, or tau ν_τ neutrino. With the original detectors only being able to detect the ν_e, this would result in a flux deficit (non-detection of ν_μ and ν_τ). This oscillation amongst three flavors was given the name the 'MSW effect' after Mikheev & Smirnov (1986) and Wolfenstein (1978), and later confirmed experimentally by the SuperKamionkande experiment.

The neutrino experiments together with the standard solar model SSM provide much of what we know about the solar energy generation and the solar core. They imply a temperature of 15.6×10^6K and density of $1.48 \times 10^5 \, \text{kg} \, \text{m}^{-3}$ at solar centre, and also confirm the existence of a variety of pp reactions (pp 1 to

pp IV), and some level of Carbon-Nitrogen-Oxygen (CNO) fusion process. These fusion processes occur over $0.0 - 0.25\,R_{\odot}$ (Figure 1.1), which defines the solar core. Outside the core the temperature drops to a value such that fusion ceases. While thermonuclear fusion is the third aspect of the SSM involves the generation of solar energy, the fourth aspect involves exactly what happens to this energy once it is generated i.e., it describes an energy transport mechanism.

Beyond $0.25\,R_{\odot}$ the temperature drops to 8 MK, such that fusion stops but only free protons and electrons exist. In this environment, the photons continuously scatter off free particles, undergoing a random walk toward the surface over a distance of $0.25 - 0.7\,R_{\odot}$. This region is known as the radiative zone and has densities of $2 \times 10^4 - 2 \times 10^2\,\mathrm{kg\,m^{-3}}$, resulting in a small photon mean free path (mfp) of $9.0 \times 10^{-4}\,\mathrm{m}$. The photons proceed towards the solar surface over a very long time scale, taking on the order of 10^5 years to traverse this region (Mitalas & Sills, 1992). If radiative energy transport occurs, it will result in the following temperature gradient

$$\frac{dT}{dr} = -\frac{3}{16\sigma}\frac{\kappa\rho}{T^3}F_{rad} \tag{1.5}$$

where σ is the Stefan-Boltzman constant, κ is the mass extinction coefficient (opacity per unit mass), ρ is mass density, T is temperature, and F_{rad} is the outward radiative flux. This implies that for a particular outward flux, if the opacity increases, a steeper temperature gradient is required to maintain such a flux. At $0.7\,R_{\odot}$ the temperature drops to $1\,\mathrm{MK}$ allowing protons to capture electrons into a bound orbit. The existence of electrons in atomic orbit results in a dramatic increase in opacity of the plasma (Turck-Chièze & Couvidat, 2011) and hence the temperature gradient increases. The increased temperature gradient required to sustain the energy flow may lead to the onset of a convective instability beyond $0.7\,R_{\odot}$ toward the solar surface. This instability will occur if the temperature gradient in the star is steeper than the adiabatic temperature gradient

$$\left|\frac{dT}{dr}\right|_{star} > \left|\frac{dT}{dr}\right|_{adiabatic} \tag{1.6}$$

This is known as the Schwarzschild criterion, and it is fulfilled from $0.7 - 1\,R_{\odot}$ −a region known as the convection zone. The temperature and density drop as
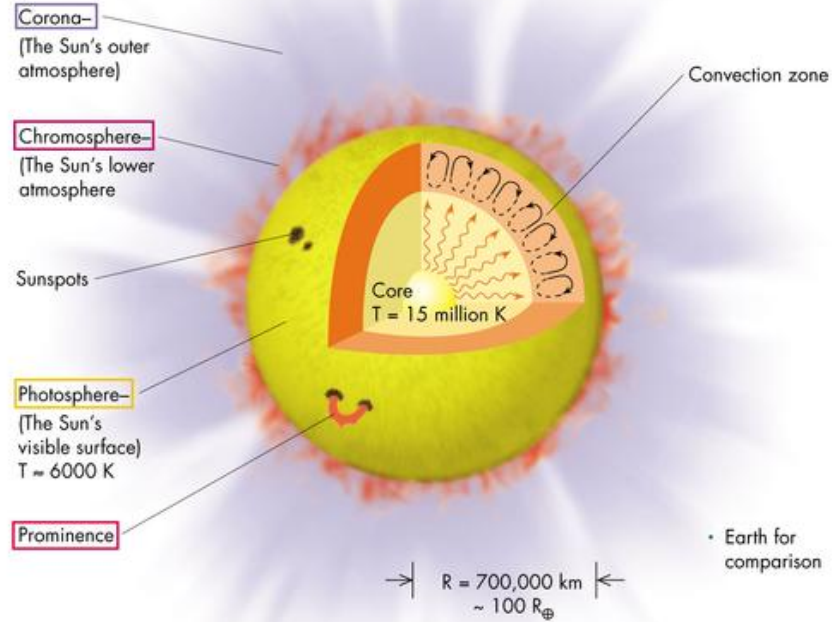
Figure 1.1: The internal structure of the Sun, including the core, radiative zone, and convective zone. Also shown is the structure of the its atmosphere, including the photosphere, chromosphere, and corona. The layers of the solar atmosphere are usually demarcated by temperature changes as height above the solar surface increases. The temperature ranges from ∼6000 K in the photosphere to above 1 MK in the corona.

height increases and finally reaches T∼6000 K and mass densities of $\rho \sim 1 \times 10^{-5} \, \mathrm{kg \, m^{-3}}$. Although no complete theoretical treatment of convection exists, mixing length theory and hydrodynamical modeling are used to determine how convection occurs in the solar interior. Convection ceases at $1 \, R_\odot$, where the environment makes a sudden transition to convectively stability. At this point the opacity drops and energy is released in the form of radiation, demarcating the start of the solar surface, known as the photosphere.

Much of what we know about the depth, temperature, and density of the convection zones come from a fine-tuning of the standard solar model, such that the model reproduces observations from neutrino and helioseismology experiments. In fact helioseismology alone can indicate great detail of the internal structure of
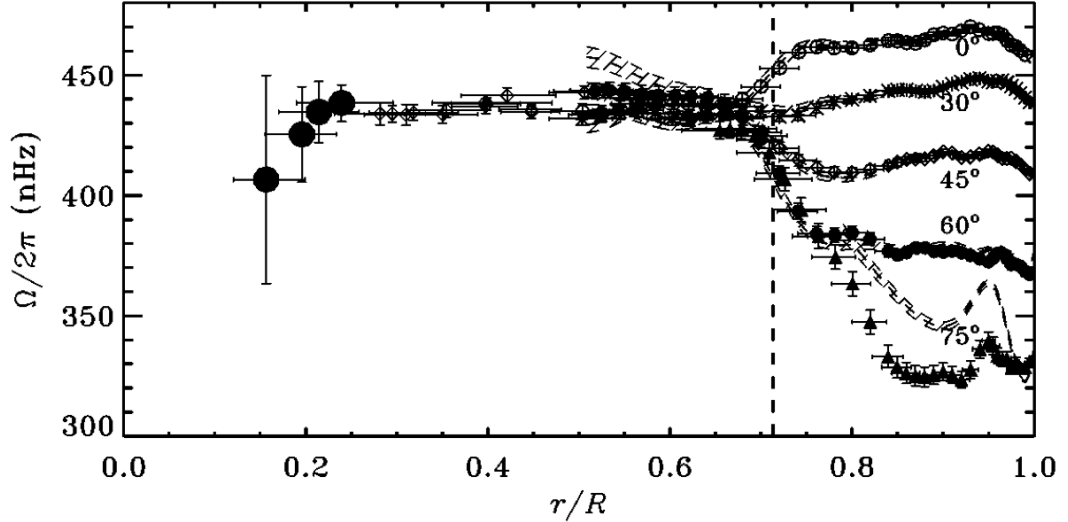
Figure 1.2: Helioseismological determination of interior rotation rate in nanoHertz (nHz) as a function solar radius, starting from solar centre ($r = 0.0$) to surface ($r = 1.0$). The separate symbols show different latitudes, from 0° to 75°. The data show that the interior rotates differentially down to $\sim 0.7\,R_\odot$. The dashed line demarcates the boundary between solid body rotation and differential rotation (Thompson *et al.*, 2003).

the Sun. This field makes use of the fact the Sun acts as a resonator for acoustic waves which manifest as detectable oscillations in the doppler shift of photospheric Fraunhofer lines. These acoustic waves are referred to as pressure or p-modes, and a variety of wavelengths exist. Wavelengths that are an integer multiple of of the solar cavity may exist as standing wave modes. Such wave modes have a period of approximately 5 minutes (Turck-Chièze & Couvidat, 2011).

The shorter wavelengths in the mode propagate into the solar convection zone and experience a total internal reflection at a shallow depth, while longer wavelengths can penetrate into much deeper layers. Hence depending on the period observed, the oscillations provide a probe of the internal thermodynamic properties at a particular level. Once such property closely monitored is the sound speed, which is seen to match the predicted sound speed based on the standard model. However, the observation and prediction show the biggest deviation at a depth of $0.3\,R_\odot$, which is the region where the radiative zone transitions to the

convective zone. This obviously implies that SSM is lacking in its description of how the solar interior is stratified at this depth. This partly due to the fact the SSM does not take into account differential rotation. The solar surface rotates faster at the equator than it does at the poles i.e., angular velocity is stratified with latitude. Helioseismology has revealed that such differential rotational continues to the bottom of the convection zone. In the deeper radiative zone and core the Sun rotates as a solid body see Figure 1.2. There is a dramatic change in the internal dynamics when transitioning from convective to radiative zones.

As predicted by sound speed measurements and differential rotation, the region sandwiched in between radiative and convective zones is and extremely important boundary. It is known as the tachocline, and the dynamics of this thin layer is believed to play and extremely important role in the generation and evolution of the solar magnetic field (Thompson *et al.*, 2003).

1.1.2 Solar Magnetic Field and Dynamo

The solar magnetic field is the ultimately source of all energetic activity in the its atmosphere. At solar activity minimum the solar magnetic field has a poloidal dipolar structure, with the polar axes generally being coincident with the rotational axes. However as the the activity cycle progresses towards a maximum, the field gains a strong toroidal component, making it far more dynamic and complex. This complex toroidal component manifests at the surface as sunspots, hence the number of sunspots on disk has been used as a proxy for the activity cycle for over 100 years, often showing an approximate 11 year periodicity (Figure 1.3, bottom panel). At the beginning of the cycle sunspots tend to appear on disk with a latitudinal distribution of $\pm 30°$ of the equator. As the cycle progresses, sunspots appear at lower and lower latitude (known as Spörer's law), until they eventually disappear at the end of a cycle. Sunspot latitude with respect to time is shown in Figure 1.3, top panel, and is known as the butterfly diagram.

Sunspots in there simplest case emerge as a dipole structure, with the leading spot being closer to the equator, such that the dipole is titled relative to the solar equator (Joy's law). In a given hemisphere, the leading sunspot and trailing spot have opposite polarities, with the polarities reversed in the other hemisphere
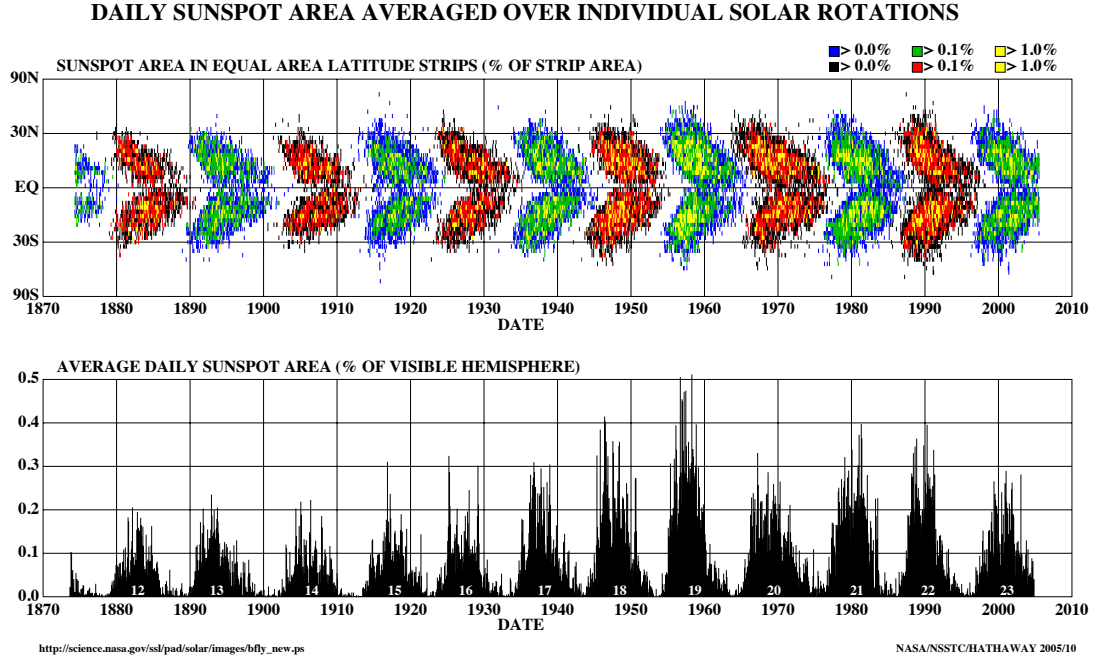
Figure 1.3: Top: The latitude of sunspots as a function of time. During the rise phase of each cycle the sunspots have a latitudinal distribution of $\pm 30°$ from the equator. As the solar cycle progresses, sunspots emergence takes place at an increasingly lower latitude. Bottom: Sunspot area as a function of time. The approximate 11 year periodicity is clearly shown.

(Hayle's law). The trailing polarity can often be more fragmented and dispersed that the leading polarity. Despite sunspots generally having a dipolar structure, spot groups can be far more complex, having a multipolar structure (this will be described more later).

Over the course of a solar cycle, the sun changes polarity (at the time of sunspot maximum). For example, an overall dipolar configuration of North-South will become South-North, another cycle will bring it back to N-S once more. While the activity cycle usually last 11 years, one full magnetic cycle has a period of 22 years.

The complex behavior of the solar magnetic field over an 11 year activity cycle, during which the dipole flips, is generally explained by solar dynamo the-
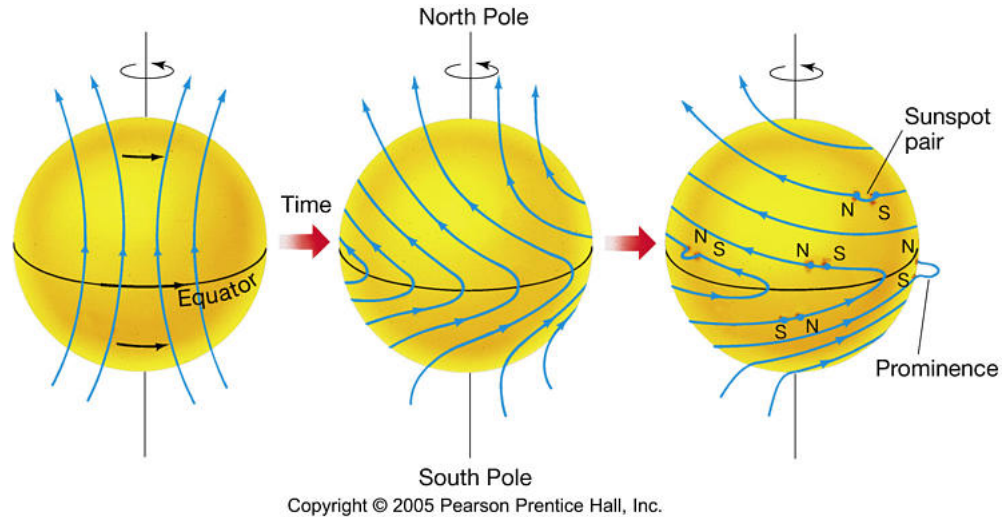
Figure 1.4: Differential rotation and flux freezing result in the poloidal dipolar magnetic field, generated by dynamo action, to be dragged around in a toroidal direction, an action known as the omega effect. Buoyancy of the field lines results in them rising and twisting, known as the alpha effect, eventually surfacing to become bipolar fields that extend far into the corona.

ory. This involves large-scale flow patterns of the solar interior that act to both induct and diffuse the magnetic field such that it produces the familiar 11 year magnetic activity cycle. Magnetohydrodynamics (MHD) is employed such that the magnetic induction equation and velocity field equation (equation of motion) are solved in numerical models to produce a toroidal field from a poloidal one, a process known as the Ω-effect. The theories must adhere to the constraints provided by observations of the sunspot cycle (Spörer's, Joy's, and Hale's laws), and also helioseismology observations of how the interior is structured.

Babcock (1961) first proposed a mechanism whereby the differential rotation of the solar convection zone tends to drag the field from a poloidal position into a toroidal one, eventually winding the field into a a stressed state, see Figure 1.4. The main storage of this wound field is in the region below the convection zone known as the tachocline. This region is known as an 'overshoot' layer, in which descending convective flows are a trapped due the subadiabicity of the region (convectively stable). This stability allows field to be built up and stored into complex magnetic structures. Parts of this structure may form a twisted mag-

netic 'flux-rope', and due to it's excess magnetic pressure, it becomes convectively unstable and begins to rise. During this rise a Coriolis force has a tendency to tilt into a north-south orientation and eventually penetrate through the solar surface and into the atmosphere, known as the α-effect (the tilt from Coriolis effects explains Joy's law). Dynamo theory attempts to explain the Ω-effect wrapping and build up of toroidal flux in the solar interior via inductive plasma flows (Charbonneau, 2010), particularly using the observed flow structure from helioseismology. Further MHD of convective instabilities is employed to describe the α-effect rise of flux systems into the solar atmosphere from the stably convective tachcoline/overshoot layer. This is very much a study in itself, and describes the eventual formation coronal active regions from sub-photospheric flux-systems (Fan, 2009).

1.1.3 Solar Atmosphere

The solar atmosphere begins above the visible surface of the sun, known as the photosphere. At this point, the Sun become optically thin to visible radiation and light escapes from this surface. Beyond this visible surface is the solar chromosphere, the corona, which eventually becomes the solar wind. Each of these layers is home to a complex array of phenomena, and each layer with it's accompanying attributes is described here.

1.1.3.1 Photosphere

As mentioned the photosphere begins where the atmosphere become optically thin. 'Visible light' in this instance is usually taken to mean light with a wavelength of $5000\,\text{Å}$, hence the emergent light from the photosphere is taken to come from the surface at which $\tau_{5000} = 2/3$. This is a consequence of the Eddington-Barbier approximation, and says that emergent flux F_ν from the photosphere is given by

$$F_\nu = \pi B_\nu(\tau = 2/3) \tag{1.7}$$

e.g., the emergent flux is given by π times blackbody intensity at an optical depth of 2/3, where blackbody intensity B_ν is given by Planck's law

$$B_\nu = \frac{2h\pi\nu^3}{c^2}\frac{1}{\exp(h\nu/k_BT)-1} \tag{1.8}$$

where h is Planck's constant, ν is frequency, c is the speed of light, k_B is Boltzmann's constant, and T is temperature. Integrated over frequency this results in $F = \sigma T^4(\tau = 2/3)$, where the frequency integrated flux is proportional to the temperature at $\tau = 2/3$, hence the effective temperature of solar blackbody radiation is $T_{eff} = T(\tau = 2/3) = 5800\,\mathrm{K}$. Solar radiation at visible wavelengths is most closely characterised by a blackbody of temperature 5800 K, although the brightness temperature T_B the solar photosphere can deviate from this value, since not all frequencies emerge from the same optical depth.

The visible appearance of the photosphere reveals a small scale granular structure, with granules of typical size scale of $1000\,\mathrm{km}$ with a lifetime of 5-10 minutes. The granules typically show bright centers surrounded by darker intergranular lanes. Doppler measurements reveal that granule centres have a positive (upward) velocity of up to $\sim 1\,\mathrm{km\,s^{-1}}$, with intergranular lanes having a negative (downward) velocity. Such upward and downward flow reveals that granulation at the photosphere are the surface manifestation of convective activity in the deeper layers of the sun, although the size scales of granules are much smaller than the convective plumes believed to permeate the convection zone. As well as the conspicuous granulation at the photospheric surface there is also a much larger scale 'super-granulation' which has much the same mechanism as the granules e.g, upflows at granule centre and downflows at the edges in the granular network. The flow speeds are much slower with typical speeds of $0.1\,\mathrm{km\,s^{-1}}$. The have a much larger size of $10,000 - 30,000\,\mathrm{km}$ and longer lifetimes of several days. They have an important role in the build up and concentration of magnetic flux in the intergranular lanes. Apart from, granules and supergranules, the most conspicuous features of the photosphere are sunspots. As discussed in the previous section, these are the surface manifestation of concentrated magnetic flux that has penetrated from the solar convective zone into the solar atmosphere. The spots have a temperature of $\sim 4000\,\mathrm{K}$, which is cooler than the typical solar

blackbody temperature of 5800 K. The spots have typical magnetic field strengths of on the order of kilo-Gauss, and have an important role to play in solar activity.

Although the the intensity of the Sun in the visible may be approximated closely by a blackbody continuum, there are also the presence of dark absorption or Fraunhofer lines in the spectrum. The most notable of which are the H-alpha and CaII H and K lines. The presence of these lines reveals that cooler part of the photosphere must overly the hotter base at $\tau_{5000} = 1$ (Phillips *et al.*, 2008). In fact, the variety of lines that are produced in the solar atmosphere (both emission and absorption) are used to determine the temperature and density stratification of the solar atmosphere. That has most notably been done in the models of (Fontenla *et al.*, 1988; Gabriel, 1976; Vernazza *et al.*, 1981), whereby a temperature and density profile of the solar atmosphere is used to calculate the emergent intensity, using radiative transfer theory. This temperature and density profile is adjusted until the the modeled emergent intensities match the observed ones. The results of this these models is shown in Figure 1.5. From this Figure we see that there is a temperature minimum at $\sim$500 km above the photosphere where the temperature drops to $\sim$4400 K. Beyond this point the temperature begins to rise again, eventually showing a rapid increase at $\sim$2000 km. The region between the temperature minimum up the height at which temperature begins to rise rapidly is known as the chromosphere[1].

1.1.3.2   Chromosphere

- Appearance, Supergranular Network, Bright Points, Spicules, Filaments, Plage etc.

- Emission lines, H-alpha, CaII H & K.

- Temperature, Density, Opacity.

- Magnetic field strength.

At $\sim$500 km above the $\tau_{5000} = 1$ surface the temperature drops to a minimum of $\sim$4400 K. Beyond this minimum the temperature begins to rise again,

---

[1]These boundaries can vary, depending on the phenomenon observed e.g., spicules are chromospheric phenomenon which can extend far beyond the upper boundary of $\sim$2000 km
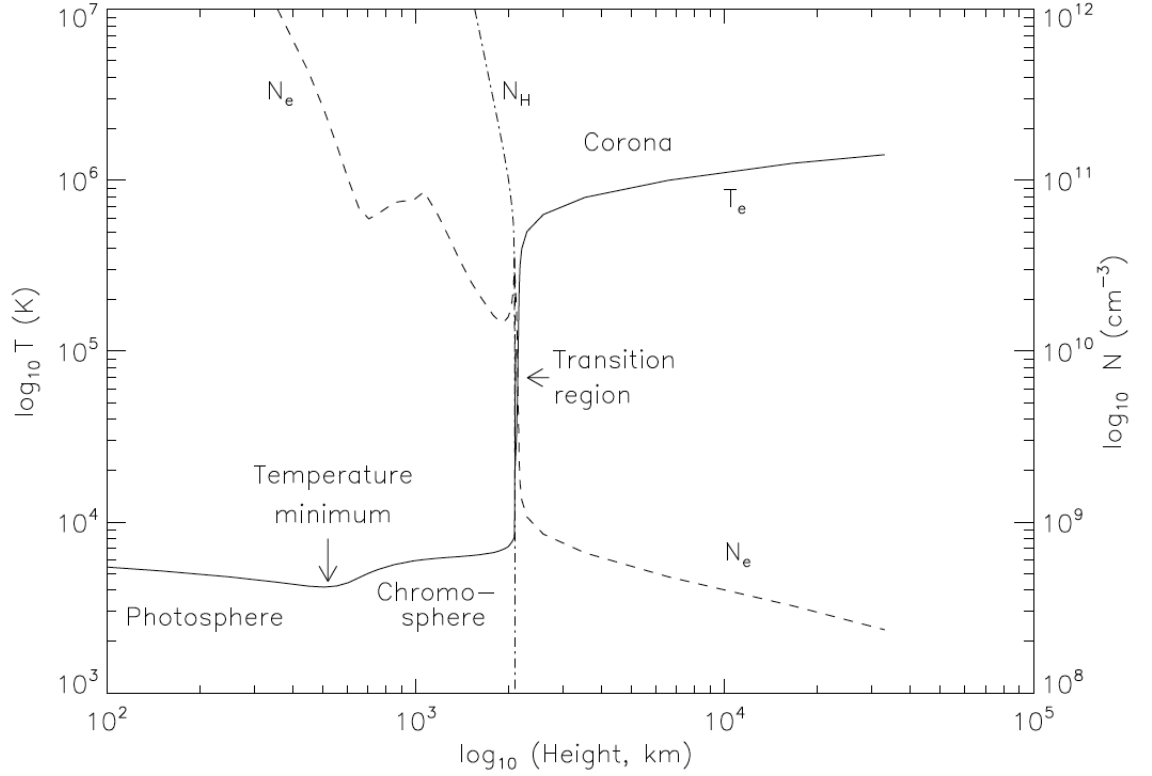
Figure 1.5: Temperature and density variation in the solar atmosphere constructed from the models of (Fontenla *et al.*, 1988; Gabriel, 1976; Vernazza *et al.*, 1981), adopted from (Phillips *et al.*, 2008).

demarcating the beginning of the chromosphere. This layer of the atmosphere is generally accepted to extend to a height at which temperatures reach 20,000 K, however temperatures as high as $\sim 1 \times 10^5$ K are sometimes attributed to chromospheric heights, hence it is observable at ultraviolet (UV) wavelengths as well as visible.

1.1.3.3 Corona

- Appearance UV: Active regions, Coronal Loops, Holes.

- Emission lines, Mg, Ca, Fe, C, O etc.

- Appearance White-Light: Streamers, K, F, E corona

- Appearance Radio: thermal bremsstrahlung, free-free emissivity/opacity.

- Temperature, Density, Opacity, 'coronal heating problem'.

At a height of approximately 2,000 km the temperature begins to rise sharply while the number density of neutral hydrogen and electrons fall by several orders of magnitude. This rapid increase in temperature in such a short spatial extent (<100 km) is known as the transition region. It has a temperature on the order of 10^5 K and separates the relatively low temperature chromosphere and the high temperatures of > 1 MK in the corona. The reason for this rapid increase in temperature is still a hotly debated subject and a coronal heating mechanism remains largely unknown, this is known as the 'coronal heating problem'.

Element abundances in the corona show there is a similar composition to the photospheric abundances, with He, C, N, and O having the same ratios relative to H in the corona as that in the photosphere. The only difference is an enhancement in the abundance of low First Ionization Potential (< 10 eV) elements in the corona relative to the photosphere. For example, elements such as Na, Mg, Al, Si, Ca, Ni, and Fe can be up to three times more abundant in the corona (Feldman & Widing, 2003). The reason for the enhancement of low FIP elements in the corona is still unknown, however several models have suggested ion-neutral separation in the chromosphere by diffusion across magnetic fields, followed by transport of these ions into the corona may be viable mechanism (Geiss, 1985).

1.1.4 Solar Wind

- Parker's solution

- Parker Spiral

- Fast solar wind, Alfvén wave driver

- Mass loss rates (later compare CME mass loss)

1.2 Coronal Mass Ejections and Coronal Shocks

1.2.1 CMEs

- Appearance, white-light Illing, Hundhausen, Vourlidas

- Kinematics, velocity, acceleration

- Dynamics, masses, energies, forces

- Observations at other wavelengths, EUV, radio, SXR.

1.2.2 CMEs and Shocks

- Radio bursts, Type II, Type III

- Radio imaging of shocks

- Relationship to EUV waves, Moreton waves

1.2.3 Open Questions

2

Coronal Mass Ejection and Plasma Shock Theory

2.1 Plasma Physics and Magnetohydrodynamics

2.1.1 Maxwell's Equations

$$\nabla \cdot E = \frac{\rho}{\epsilon_0} \tag{2.1}$$

$$\nabla \cdot B = 0 \tag{2.2}$$

$$\nabla \times E = -\frac{dB}{dt} \tag{2.3}$$

$$\nabla \times B = \mu_0 j + \frac{1}{c^2}\frac{dE}{dt} \tag{2.4}$$

2.1.2 Plasma Physics and Boltzmann Equation

2.1.3 Magnetohydrodynamics

2.1.4 Magnetic Reconnection

2.1.5 MHD Rankine-Hugoniot Equations

2.1.6 Bow Shocks

2.2 Coronal Mass Ejections

2.2.1 Catastrophe Model

2.2.2 Magnetic Breakout Model

The magnetic breakout model was first proposed by (Antiochos *et al.*, 1999) and involves a quadrupolar (or more complex) magnetic flux system. A core magnetic flux is flanked by two side-lobe flux systems. The core and two side lobes lie underneath a field that provides a tension, stabilizing the entire system. Above the core flux there is a magnetic null point. Non potentiality is injected into the core flux by twisting/shearing of the magnetic footpoints or flux emergence. This non-potentiality causes the core flux to grow and encounter the overlying field creating the tension. Contact of the core flux and overlying flux creates a current sheet above the core, allowing reconnection to occur. This reconnection removes flux from the overlying field and adds it to the side-lobe flux systems, allowing the core flux to escape. The magnetic breakout model was used to circumvent the Aly-Sturrock limit (reference) i.e., it allowed a flux system to erupt, without having to open the constraining field lines to infinity. There has been observational tests of the magnetic-breakout model, showing it to be a viable explanation of some flaring and CME events. The most notable of these is the Bastille Day event (reference Amarai).The obseronal signatures of the model include the presence of a null point in the corona above a complex quadrupolar flux system (inferred from potential field source surface extrapolations), a radio source imaged to be above the erupting structure (implying a reconnection site), and radio bursts beginning at frequencies indicative of high altitude (again indicating energy release above the erupting structure, prior to eruption) - reference
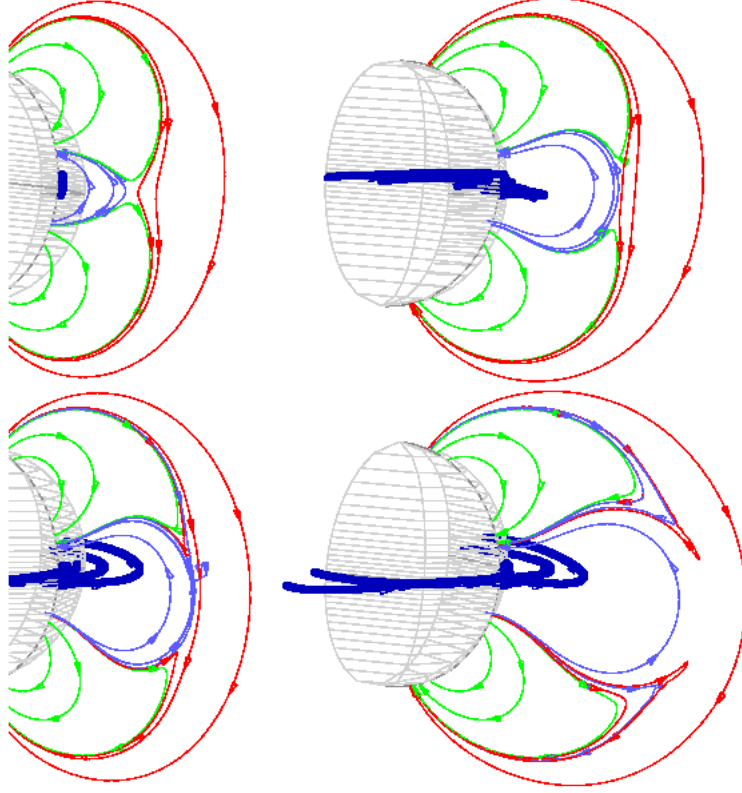
Figure 2.1: The breakout model, consisting of a quadrupolar flux system in which the central flux (blue) is flanked by to side lobe flux systems (green), with the entire system kept in stability by the tension of the overlying red field. Shearing and/or twisting on the underlying flux causes it to grow slowly. Eventually a current sheet forms at the magnetic null above the central flux, causing reconnection. This reconnection transfers overlying field to the side-lobes, effectively creating a conduit for the central flux to escape as a CME.

Manoharan. However, in some instances magnetic breakout is implied by observations of the above, but the kinematics are inconsistent with model predictions. For example the model predicts a long slow rise of the central flux system as the underlying field is increasingly sheared. The CME/central flux begins rapid acceleration once breakout reconnection is initiated. However, in the study of

Bong *et al.* (2006) the breakout reconnection occurred at the end of the CME acceleration phase, prompting a two-phase acceleration scenario.

Kinematcally the CME/central flux system should experience a slow rise (1 km/s) for several hours due to shearing/twisting of the footpoints. Once breakout reconnection has begun the CME experiences a much larger acceleration (100 km/s) for ~ 1 hour. The transference of magnetic flux to the side lobes drives the flare and is the source of energetic particles that lead to flare hard X-rays and ultimately soft X-rays. Therefore magnetic breakout predicts that the flaring process and SXR peak should only begin after CME acceleration (after breakout reconnection) (Lynch *et al.*, 2004). However, the precedence is breakout reconnection over flaring reconnection may not always be case, with latter sometimes driving the former (MacNeice *et al.*, 2004)

2.2.3   Toroidal Instability

The toroidal instability model incorporates a pre-existing flux rope structure that is built from a torus of magnetic flux, some of which is buried beneath the photosphere (Chen, 1989). The flux system is can be broken down into a combination of toroidal magnetic, toroidal current and a poloidal magnetic field and current Figure 2.2. This flux rope system is embedded in a surrounding coronal magnetic field B_{corona}. The stability of the system depends on the nature of the $J \times B$ force due to the interaction toroidal and poloidal components of both the field and current. The interaction of J and B internal to the flux rope is usually termed the Lorentz self-force or the 'hoop' force. An instability may be induced via twisting of the fluxrope footpoints to increases the amount of poloidal flux (effectively increasing the helicity of the system). Once the instability is induced, the fluxrope begins a bulk motion as well as a growth in its semi-minor axis. Hence the motion of the system can be analysed by looking at the central axis or the minor axes (leading and trailing edges. The three axes display slightly different kinematics e.g., the leading edge has a faster velocity than the trailing edge (due to fluxrope expansion). this has proved a useful test of the model when comparing the observations of erupting fluxrope structures as seen in white-light
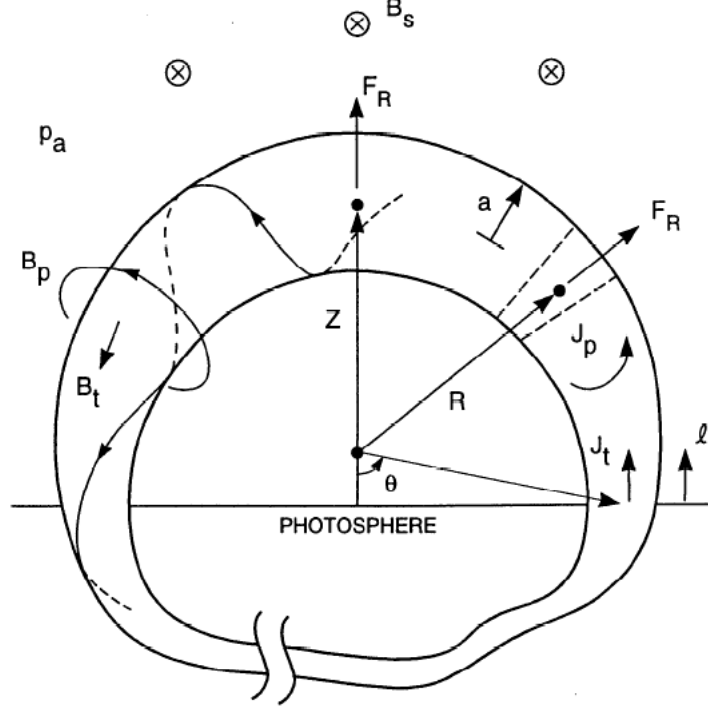
Figure 2.2: The flux rope model of Chen (1989), used to to study the toroidal instability of a twisted flux system in the corona.

coronagraphs. Krall *et al.* (2001) looked at the leading a trailing edges of erupting flux ropes, as well as the rope aspect ratio, an compared the observations to model expectations. Good agreement is found between the model kinematics and aspect ratio and the observed events. The equation of motion of the entire system is given by

$$M\frac{d^2Z}{dt^2} = \frac{I_t}{c^2 R} \times \left[\ln\left(\frac{8R}{a}\right) - 1 + \frac{\xi_i}{2} + \frac{\beta_p}{2} - \frac{B_t^2}{B_{pa}^2} - \frac{2RB_{\perp c}}{aB_{pa}}\right] - F_g - F_{drag} \quad (2.5)$$

where I_t is the toroidal current, R is the flux rope major radius, a is the rope minor radius, ξ_i is internal inductance of the flux system, B_t is the toroidal field, B_{pa} is the poloidal field at a, $B_{\perp c}$ is the perpendicular component of the ambient coronal field, F_g is the force due to gravity, F_{drag} is the drag force, M is the mass per unit length of the rope, and Z is the rope axis height above the photosphere.

The equation of motion shows that an increase in the toroidal current (or poloidal flux) contributes positively to the acceleration. The terms in the square brackets are each unitless and take into account the rope geometry, self-inductance and interplay between poloidal and toroidal flux. The first three terms in the square brackets are what give rise to the hoop-force. If the rope is mass loaded with a prominence, this can contribute to the rope's stability via the gravity term. The drag term only becomes an important contributor to rope dynamics later in the propagation, when the solar wind speed begins to increase i.e., at around $10R_\odot$ reference Sheeley. The eruption is driven by flux-injection, which typically lasts for 4-8 hours, during which time the unstable system loses its equilibrium and begins to rise Krall *et al.* (2001).

It is significant the fluxrope is already established in the corona before eruption begins i.e., the rope formation is not addressed in the model and it is not a consequence of eruption. Hence magnetic reconnection is not a necessary aspect of the model and the eruption may proceed without employing resistive MHD.

2.2.4   Drag Models

2.3   Coronal Shocks and Plasma Emission

2.3.1   Shock Particle Acceleration

2.3.2   Wave-Particle Interaction

Quasi-linear relaxation

2.3.3   Three-Wave Interaction and Plasma Emission

Once the Langmuir waves are produced from the bump-on-tail instability a number of wave interaction processes occur in order to bring about plasma emission. This involves the interaction of various wave modes in the plasma described by a mathematical formalism called the three-wave interaction. In this process three wave modes in a plasma M, P, and Q are described by their distribution functions in a wave-number space (k-space). the distribution functions are given by $N_M(k_M)$, $N_P(k_P)$, $N_Q(k_Q)$, where the N describe the occupation number of wave
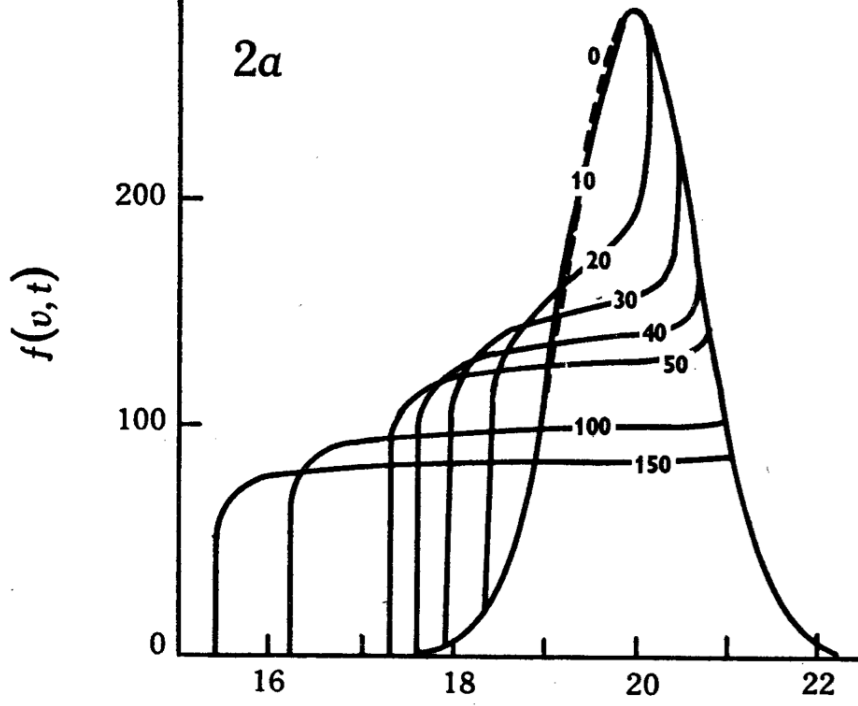
quanta between k and $k + dk$ in the wave-number space. Waves in P and Q mode may interact to such that wave quanta are removed from the P and Q k-space and added to the M k-space. This is essentially an emission of an energy packet from the P and Q -space to the M k-space. The rate of change of occupation numbers in the three k-spaces are given by

$$\frac{dN_M(\mathbf{k}_M)}{dt} = -\int \frac{d^3\mathbf{k}_P}{(2\pi)^3} \int \frac{d^3\mathbf{k}_Q}{(2\pi)^3} g(\mathbf{k}_M, \mathbf{k}_P, \mathbf{k}_Q) \tag{2.6}$$

$$\frac{dN_P(\mathbf{k}_P)}{dt} = -\int \frac{d^3\mathbf{k}_M}{(2\pi)^3} \int \frac{d^3\mathbf{k}_Q}{(2\pi)^3} g(\mathbf{k}_M, \mathbf{k}_P, \mathbf{k}_Q) \tag{2.7}$$

$$\frac{dN_Q(\mathbf{k}_Q)}{dt} = -\int \frac{d^3\mathbf{k}_M}{(2\pi)^3} \int \frac{d^3\mathbf{k}_P}{(2\pi)^3} g(\mathbf{k}_M, \mathbf{k}_P, \mathbf{k}_Q) \tag{2.8}$$

where $g(\mathbf{k_M}, \mathbf{k_P}, \mathbf{k_Q})$ is incorporates a transition probability for wave quanta into and out of energy states in the various k-spaces (Robinson *et al.*, 1994). The

transition probability is given by

$$g(\mathbf{k}_M, \mathbf{k}_P, \mathbf{k}_Q) = u_{MPQ}(\mathbf{k}_M, \mathbf{k}_P, \mathbf{k}_Q)[N_M(\mathbf{k_M})N_P(\mathbf{k_P})-$$
$$N_P(\mathbf{k_P})N_Q(\mathbf{k_Q}) + N_Q(\mathbf{k_Q})N_M(\mathbf{k_M})] \quad (2.9)$$

where $u_{MPQ}(\mathbf{k_M}, \mathbf{k_P}, \mathbf{k_Q})$ is the transition probability from states in P and Q to M, for example (Melrose, 1986). u_{MPQ} is analogous to transition probabilities given by the Einstein coefficients for transferring energy packets from and atomic state to a photon state (photon emission) i.e., whereas the Einstein coefficients are used in atom-wave (atom-photon) energy exchanges, u_{MPQ} describes wave-wave energy exchanges. The transition probability is given by

$$u_{MPQ}(\mathbf{k}_M, \mathbf{k}_P, \mathbf{k}_Q) \propto \delta(\omega_M - \omega_P - \omega_Q)\delta^3(\mathbf{k}_M - \mathbf{k}_P - \mathbf{k}_Q) \quad (2.10)$$

where the ω are the frequency of the corresponding wave and and δ are delta functions. Given the presence of delta functions in the transition probability expression, we can see that an exchange of energy quanta amongst the wave modes can only occur when

$$\omega_M = \omega_P + \omega_Q \quad (2.11)$$
$$\mathbf{k}_M = \mathbf{k}_P + \mathbf{k}_Q \quad (2.12)$$

Hence for an a conversion wave modes in a plasma such as $M \to P + Q$ (a decay of mode M into P and Q), or it's reverse process $P + Q \to M$ (a coupling of P and Q to produce M) is described by equations (2.1) to (2.7).

The production of plasma emission after a bump-on-tail instability has occurred requires a three wave interaction amongst a Langmuir wave L, ion acoustic wave S, and electromagnetic wave T. Fundamental emission during a radio burst occurs via a decay of Langmuir waves into an electromagnetic and ion sound wave

$$L \to T + S \quad (2.13)$$

while second harmonic first requires the decay $L \to L' + S$, where L' is a product Langmuir wave propagating in the opposite direction to the first. This is followed

by a coalescence of the original and product Langmuir waves

$$L + L^{'} \rightarrow T'$$ (2.14)

- The dispersion relations

- Source emissivities

3

Observation and Instrumentation

3.1 Thompson Scattering Theory

3.1.1 Thomson Scattering in the Corona

The tangential component (I_T), radial component (I_R), and polarization (I_P) of the scattered intensity are given by the expressions

$$I_T = I_0 \frac{\pi \sigma_e}{2z^2} [(1-u)C + uD] \tag{3.1}$$

$$I_P = I_0 \frac{\pi \sigma_e}{2z^2} \sin^2\chi [(1-u)A + uB] \tag{3.2}$$

with $I_R = I_T - I_P$. A, B, C, and D are the van de Hulst coefficients and are a trigonometric function only of the solid angle subtended by the Sun at the scattering point (see Appendix). I_0 is incident intensity, σ_e is the electron scattering cross section, z is the distance from scatterer to observer, u is a limb darkening coefficient, and χ is the angle between a radial vector from sun centre to the scattering electron and a position vector from observer to the electron.

The total scattered intensity is given by

$$I_{tot} = 2I_T - I_p \sim I_0 \frac{\pi \sigma_e}{z^2} \left(1 - \frac{\sin^2 \chi}{2}\right) \tag{3.3}$$

The van de Hulst coefficients are solutions of a set of integrals to obtain the brightness of each component of the radiation scattered by a single electron in the solar corona. They are a result of scattering theory applied to the case of an electron receiving radiation from the entire solar disk, as opposed to a simpler point source of incident radiation. They are as follows

$$A = \cos \Omega \sin^2 \Omega \tag{a}$$

$$B = -\frac{1}{8}\left[1 - 3\sin^2 \Omega - \frac{\cos^2 \Omega}{\sin \Omega}(1 + 3\sin^2 \Omega)\ln\left(\frac{1 + sin\Omega}{\cos \Omega}\right)\right] \tag{b}$$

$$C = \frac{4}{3} - \cos \Omega - \frac{\cos^3 \Omega}{3} \tag{c}$$

$$D = \frac{1}{8}\left[5 + \sin^2 \Omega - \frac{\cos^2 \Omega}{\sin \Omega}(5 - \sin^2 \Omega)\ln\left(\frac{1 + \sin \Omega}{\cos \Omega}\right)\right] \tag{d}$$

where Ω is the angle between the lines QS and QT. Q is the scattering point, S is Sun center, and T is the point where the scattered point vector crosses the Sun at a tangent (Howard & Tappin, 2009).

3.1.2 White-light observations of CMEs

3.2 Coronagraphs

Before the early 20th century the only way to view the corona was for a short period during a solar eclipse when the moon blocks direct photospheric light. Under normal conditions direct sunlight overwhelms the faint corona. In 1939 the French Astronomer Bernard Lyot developed a telescope, known as a coronagraph, which allowed observation of the corona at any time (Lyot, 1939). A coronagraph is an optical system that provides an artificial eclipse of direct photospheric light so the much fainter corona can be imaged.
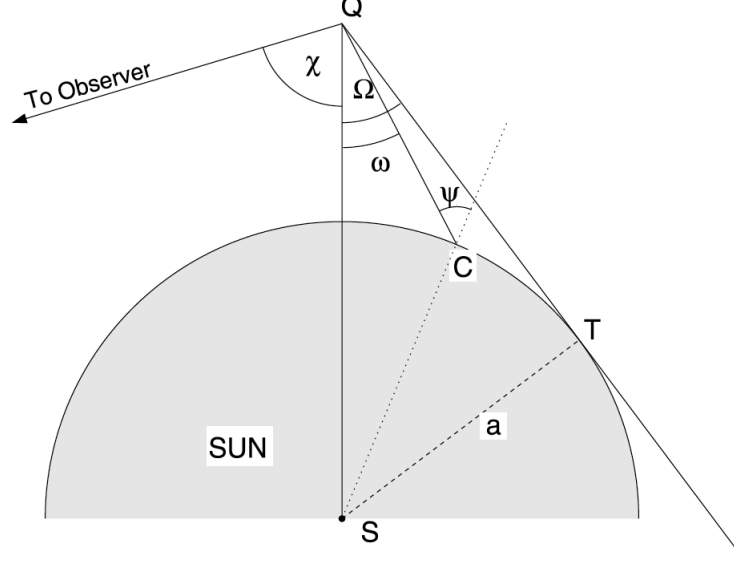
Figure 3.1: Geometry of single electron scattering in the solar atmosphere, with angles Ω and χ.

3.2.1 Lyot Coronagraph

The Lyot Coronagraph is the name given to the first optical design of a coronagraph developed by Bernard Lyot. A basic schematic of the instrument is given in Figure 3.2. The optical element O1 is a lens that is extremely polished to prevent scattering and reflections of incident light. O1 creates an image of the Sun onto its focal plane at F1 where the occulting disk, D1, reflects away the unwanted solar disk image. F1 then images the objective lens and the occulting disk onto the plane of O2. Lyot's key invention was the Lyot stop and Lyot spot. These are devices onto which light diffracted at the occulting disk is directed and subsequently blocked from being imaged by the final lens O2. O2 then images the faint corona and occulting disk onto the detector plane.

The Lyot coronagraph is described as internally occulting due to the placement of the occulting disk behind the first objective lens. This is to distinguish it from a externally occulted system in which the disk is placed in front of the objective lens. Modern coronagraphs follow the same basic design of Lyot's but contain extra features such as baffles to stop any scattered light in the telescope.

INTERNALLY OCCULTED REFRACTING CORONAGRAPH (LYOT)
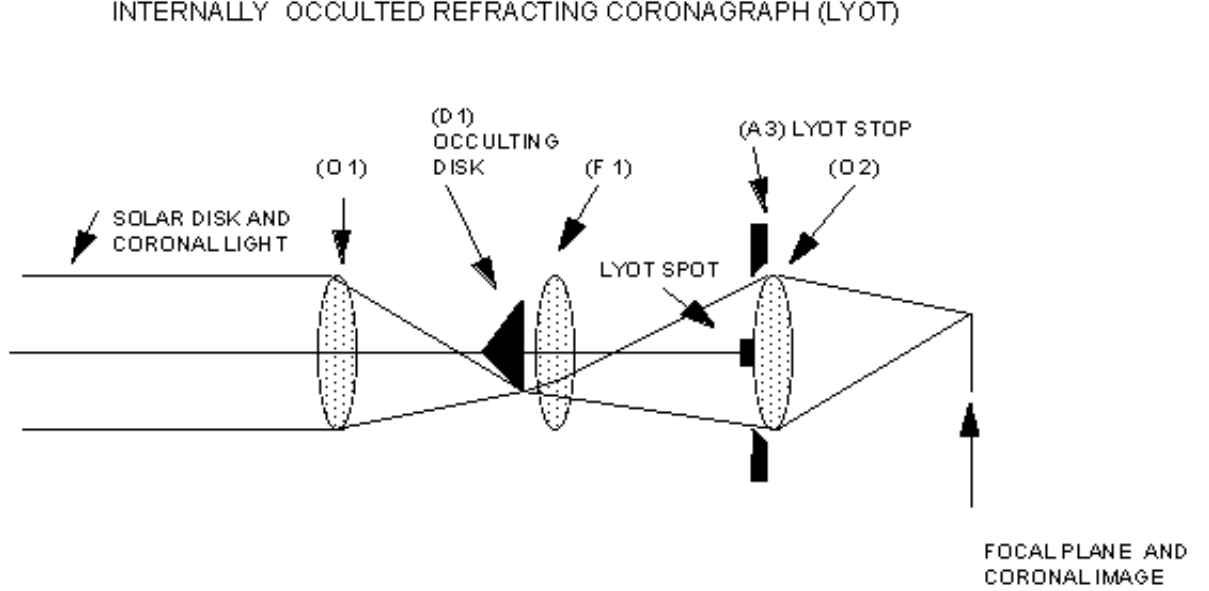
Figure 3.2: A schematic of the basic optical design of the Lyot coronagraph. Lyot's key inventions where the placement of a Lyot stop and Lyot spot at the positions where diffracted light would contaminate the image and obscure the faint corona.

3.2.2   STEREO COR1 and COR2

The *Solar Terrestrial Relations Observatory* (*STEREO*; Kaiser *et al.*, 2008) Ahead and Behind are two nearly identical spacecraft traveling ahead and behind Earth in its orbit. Each spacecraft is receding from Earth at a rate of $\pm 22°$ per year, such that they are effectively traveling around the Sun in opposite directions. They carry an identical set of instruments known as the Sun Earth Coronal Connection and Heliospheric Investigation (SECCHI) suite, including in situ detectors and a variety of imagers. On each spacecraft there are two coronagraphs, COR1 and COR2 (Howard *et al.*, 2008). The Ahead COR1 and COR2 combined with Behind COR1 and COR2 offer a stereoscopic view of the corona and any transient event taking place, such as a CME.

COR1 is an internally occulted Lyot coronagraph, see Figure 3.3. It images the inner corona with a field of view from $1.4 - 4.5\,R_\odot$ in a waveband $22.5\,\mathrm{nm}$ wide centered on the Hα line at $656\,\mathrm{nm}$. It has an internal polarizer that takes three images at $0°$, $120°$, and $240°$, so that polarized or total brightness images

of the inner corona may be produced. It nominally produces 1024×1024 pixel images with platescale of 3.75 arcsec per pixel (Thompson & Reginald, 2008). A typical observing sequence will give an image cadence of 10 minutes.

COR2 is an externally occulted Lyot coronagraph. Externally occulted coronagraphs have an extra occulting disk in front of the objective lens, see Figure 3.4. This is to prevent direct sunlight scattering off of the objective lens, making internally scattered light less of a problem for this type of coronagraph. A downside to this design is that the external occulter does not allow the inner corona to be imaged, hence such coronagraphs are usually used to observe the extended corona to larger heights. COR2 observes the corona in a field of view from $2.5 - 15\,R_\odot$ and in a wavelength range of $650 - 750\,\mathrm{nm}$. It nominally produces 2048×2048 images, with 14.7 arsec per pixel. Like COR1 it has an internal polarizer producing three linearly polarized images per observing sequence (30 minutes).

These white light imagers of the corona allow for a stereoscopic view of CMEs in a total field of view covering $1.4 - 15\,R_\odot$. The two viewpoint capabilities of these telescopes offer a more accurate observational estimation of both CME kinematics and CME mass, resulting in a better understanding of CME dynamics.

3.2.3 SOHO LASCO

3.3 Radio Spectrometers and Radioheliographs

3.3.1 RSTO Callisto

3.3.2 STEREO WAVES

3.3.3 Nancay Decametric Array

3.3.4 Nancay Radioheliograph

3.4 EUV imaging

3.4.1 SDO AIA
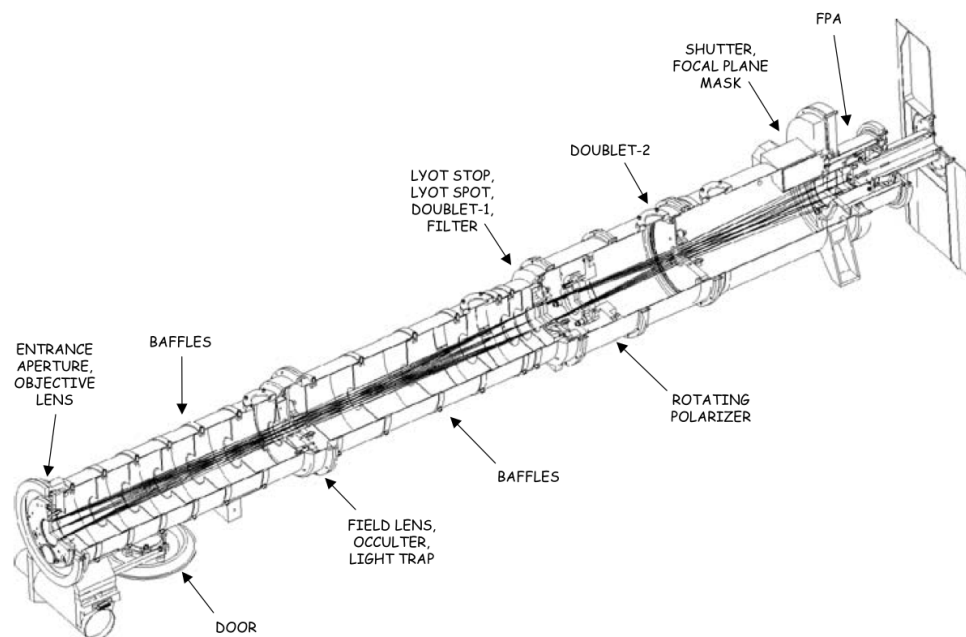
Figure 3.3: A schematic of the basic optical design of the the COR1 coronagraph. There are two such identical instruments, one on the Ahead and one on the Behind spacecraft. It is the same basic design as the Lyot coronagraph with the addition of baffles to prevent scattered light and a polarizer behind the Lyot stop (Thompson & Reginald, 2008).
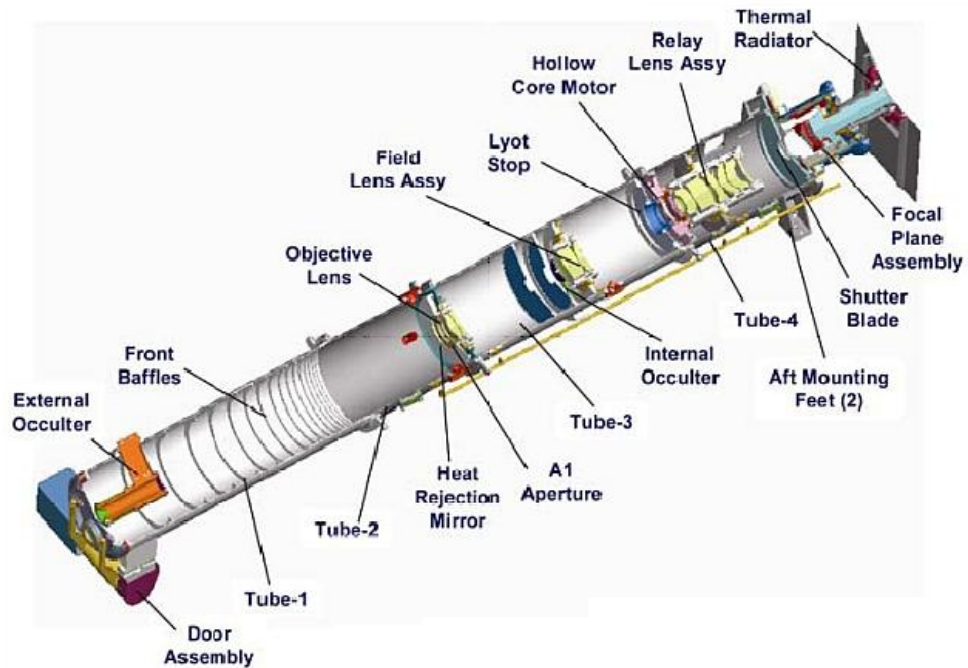
Figure 3.4: A schematic of the basic optical design of the COR2 coronagraph. This is an externally occulted coronagraph, meaning it has an extra occultation disk in front of the objective lens. This results in less internally scattered light, but also results in an obscuration of the inner corona. As with COR1, there are two such identical instruments, one on the Ahead and one on the Behind spacecraft (Howard *et al.*, 2008).

4

Coronal Mass Ejection Masses, Energetics, and Dynamics

4.1 Masses

4.1.1 Evaluation of Uncertainties

4.1.2 Masses

4.2 Energies and Dynamics

4.2.1 Mechanical Energy

4.2.2 Forces acting on CMEs

5

Coronal Mass Ejection Masses, Shocks, and Particle Acceleration

5.1   Radio Bursts

5.1.1   Type II, Type III, and Herringbones

5.2   EUV Wave and Radio Source

5.2.1   Relationship with Radio Spectra

5.3   Role of the CME

5.3.1   CME Bow Shock

5.3.2   Relationship Between CME, CBF, and Radio bursts

A

A Nice Appendix

This is where the appendix would go...

References

ANTIOCHOS, S.K., DEVORE, C.R. & KLIMCHUK, J.A. (1999). A Model for Solar Coronal Mass Ejections. *Astrophysical Journal*, **510**, 485–493. (Cited on page 18.)

BABCOCK, H.W. (1961). The Topology of the Sun's Magnetic Field and the 22-YEAR Cycle. *Astrophysical Journal*, **133**, 572. (Cited on page 10.)

BONG, S.C., MOON, Y.J., CHO, K.S., KIM, Y.H., PARK, Y.D. & CHOE, G.S. (2006). Direct Observation of Low Coronal Breakout: Does Breakout Precede or Follow Solar Eruption? *Astrophysical Journal Letters*, **636**, L169–L172. (Cited on page 20.)

CHARBONNEAU, P. (2010). Dynamo Models of the Solar Cycle. *Living Reviews in Solar Physics*, **7**, 3. (Cited on page 11.)

CHEN, J. (1989). Effects of toroidal forces in current loops embedded in a background plasma. *Astrophysical Journal*, **338**, 453–470. (Cited on pages xii, 20 and 21.)

DAVIS, R., HARMER, D.S. & HOFFMAN, K.C. (1968). Search for Neutrinos from the Sun. *Physical Review Letters*, **20**, 1205–1209. (Cited on page 4.)

FAN, Y. (2009). Magnetic Fields in the Solar Convection Zone. *Living Reviews in Solar Physics*, **6**, 4. (Cited on page 11.)

FELDMAN, U. & WIDING, K.G. (2003). Elemental Abundances in the Solar Upper Atmosphere Derived by Spectroscopic Means. *Space Science Reviews*, **107**, 665–720. (Cited on page 15.)

FONTENLA, J., REICHMANN, E.J. & TANDBERG-HANSSEN, E. (1988). The Lyman-alpha line in various solar features. I - Observations. *Astrophysical Journal*, **329**, 464–481. (Cited on pages xii, 13 and 14.)

FOUKAL, P.V. (2004). *Solar Astrophysics, 2nd, Revised Edition*. Wiley-VCH. (Cited on page 2.)

FUKUDA, Y., HAYAKAWA, T., ICHIHARA, E., INOUE, K., ISHIHARA, K., ISHINO, H., ITOW, Y., KAJITA, T., KAMEDA, J., KASUGA, S., KOBAYASHI, K., KOBAYASHI, Y., KOSHIO, Y., MARTENS, K., MIURA, M., NAKAHATA, M., NAKAYAMA, S., OKADA, A., OKETA, M., OKUMURA, K., OTA, M., SAKURAI, N., SHIOZAWA, M., SUZUKI, Y., TAKEUCHI, Y., TOTSUKA, Y., YAMADA, S., EARL, M., HABIG, A., HONG, J.T., KEARNS, E., KIM, S.B., MASUZAWA, M., MESSIER, M.D., SCHOLBERG, K., STONE, J.L., SULAK, L.R., WALTER, C.W., GOLDHABER, M., BARSZCZAK, T., GAJEWSKI, W., HALVER-SON, P.G., HSU, J., KROPP, W.R., PRICE, L.R., REINES, F., SOBEL, H.W., VAGINS, M.R., GANEZER, K.S., KEIG, W.E., ELLSWORTH, R.W., TASAKA, S., FLANAGAN, J.W.,

Kibayashi, A., Learned, J.G., Matsuno, S., Stenger, V., Takemori, D., Ishii, T., Kanzaki, J., Kobayashi, T., Nakamura, K., Nishikawa, K., Oyama, Y., Sakai, A., Sakuda, M., Sasaki, O., Echigo, S., Kohama, M., Suzuki, A.T., Haines, T.J., Blaufuss, E., Sanford, R., Svoboda, R., Chen, M.L., Conner, Z., Goodman, J.A., Sullivan, G.W., Mori, M., Hill, J., Jung, C.K., Mauger, C., McGrew, C., Sharkey, E., Viren, B., Yanagisawa, C., Doki, W., Ishizuka, T., Kitaguchi, Y., Koga, H., Miyano, K., Okazawa, H., Saji, C., Takahata, M., Kusano, A., Nagashima, Y., Takita, M., Yamaguchi, T., Yoshida, M., Etoh, M., Fujita, K., Hasegawa, A., Hasegawa, T., Hatakeyama, S., Iwamoto, T., Kinebuchi, T., Koga, M., Maruyama, T., Ogawa, H., Suzuki, A., Tsushima, F., Koshiba, M., Nemoto, M., Nishijima, K., Futagami, T., Hayato, Y., Kanaya, Y., Kaneyuki, K., Watanabe, Y., Kielczewska, D., Doyle, R., George, J., Stachyra, A., Wai, L., Wilkes, J. & Young, K. (1998). Measurements of the Solar Neutrino Flux from Super-Kamiokande's First 300 Days. *Physical Review Letters*, **81**, 1158–1162. (Cited on page 4.)

Gabriel, A.H. (1976). A magnetic model of the solar transition region. *Royal Society of London Philosophical Transactions Series A*, **281**, 339–352. (Cited on pages xii, 13 and 14.)

Geiss, J. (1985). Diagnostics of corona by in-situ composition measurements at 1 AU. In E. Rolfe & B. Battrick, eds., *Future Missions in Solar, Heliospheric & Space Plasma Physics*, vol. 235 of *ESA Special Publication*, 37–50. (Cited on page 15.)

Howard, R.A., Moses, J.D., Vourlidas, A., Newmark, J.S., Socker, D.G., Plunkett, S.P., Korendyke, C.M., Cook, J.W., Hurley, A., Davila, J.M., Thompson, W.T., St Cyr, O.C., Mentzell, E., Mehalick, K., Lemen, J.R., Wuelser, J.P., Duncan, D.W., Tarbell, T.D., Wolfson, C.J., Moore, A., Harrison, R.A., Waltham, N.R., Lang, J., Davis, C.J., Eyles, C.J., Mapson-Menard, H., Simnett, G.M., Halain, J.P., Defise, J.M., Mazy, E., Rochus, P., Mercier, R., Ravet, M.F., Delmotte, F., Auchere, F., Delaboudiniere, J.P., Bothmer, V., Deutsch, W., Wang, D., Rich, N., Cooper, S., Stephens, V., Maahs, G., Baugh, R., McMullin, D. & Carter, T. (2008). Sun Earth Connection Coronal and Heliospheric Investigation (SECCHI). *Space Science Reviews*, **136**, 67–115. (Cited on pages xii, 29 and 32.)

Howard, T.A. & Tappin, S.J. (2009). Interplanetary Coronal Mass Ejections Observed in the Heliosphere: 1. Review of Theory. *Space Science Reviews*, **147**, 31–54. (Cited on page 27.)

Kaiser, M.L., Kucera, T.A., Davila, J.M., St. Cyr, O.C., Guhathakurta, M. & Christian, E. (2008). The STEREO Mission: An Introduction. *Space Science Reviews*, **136**, 5–16. (Cited on page 29.)

Krall, J., Chen, J., Duffin, R.T., Howard, R.A. & Thompson, B.J. (2001). Erupting Solar Magnetic Flux Ropes: Theory and Observation. *Astrophysical Journal*, **562**, 1045–1057. (Cited on pages 21 and 22.)

Lynch, B.J., Antiochos, S.K., MacNeice, P.J., Zurbuchen, T.H. & Fisk, L.A. (2004). Observable Properties of the Breakout Model for Coronal Mass Ejections. *Astrophysical Journal*, **617**, 589–599. (Cited on page 20.)

Lyot, B. (1939). The study of the solar corona and prominences without eclipses (George Darwin Lecture, 1939). *Monthly Notices of the Royal Astronomical Society*, **99**, 580. (Cited on page 27.)

MacNeice, P., Antiochos, S.K., Phillips, A., Spicer, D.S., DeVore, C.R. & Olson, K. (2004). A Numerical Study of the Breakout Model for Coronal Mass Ejection Initiation. *Astrophysical Journal*, **614**, 1028–1041. (Cited on page 20.)

Melrose, D.B. (1986). *Instabilities in Space and Laboratory Plasmas*. Cambridge University Press. (Cited on page 24.)

Mikheev, S.P. & Smirnov, A.I. (1986). Resonant amplification of neutrino oscillations in matter and solar-neutrino spectroscopy. *Nuovo Cimento C Geophysics Space Physics C*, **9**, 17–26. (Cited on page 4.)

Mitalas, R. & Sills, K.R. (1992). On the photon diffusion time scale for the sun. *Astrophysical Journal*, **401**, 759. (Cited on page 5.)

Phillips, K.J.H., Feldman, U. & Landi, E. (2008). *Ultraviolet and X-ray Spectroscopy of the Solar Atmosphere*. Cambridge University Press. (Cited on pages xii, 13 and 14.)

Robinson, P.A., Cairns, I.H. & Willes, A.J. (1994). Dynamics and efficiency of type III solar radio emission. *Astrophysical Journal*, **422**, 870–882. (Cited on page 23.)

Thompson, M.J., Christensen-Dalsgaard, J., Miesch, M.S. & Toomre, J. (2003). The Internal Rotation of the Sun. *Annual Review of Astronomy & Astrophysics*, **41**, 599–643. (Cited on pages xi, 7 and 8.)

Thompson, W.T. & Reginald, N.L. (2008). The Radiometric and Pointing Calibration of SECCHI COR1 on STEREO. *Solar Physics*, **250**, 443–454. (Cited on pages xii, 30 and 31.)

Turck-Chièze, S. & Couvidat, S. (2011). Solar neutrinos, helioseismology and the solar internal dynamics. *Reports on Progress in Physics*, **74**, 086901. (Cited on pages 4, 5 and 7.)

Vernazza, J.E., Avrett, E.H. & Loeser, R. (1981). Structure of the solar chromosphere. III - Models of the EUV brightness components of the quiet-sun. *Astrophysical Journal Supplemental Series*, **45**, 635–725. (Cited on pages xii, 13 and 14.)

Wolfenstein, L. (1978). Neutrino oscillations in matter. *Physical Review Letters*, **17**, 2369–2374. (Cited on page 4.)